Catalysis Science & Technology

ROYAL SOCIETY OF CHEMISTRY

PAPER

View Article Online
View Journal | View Issue

Cite this: *Catal. Sci. Technol.*, 2025, 15, 794

Tailoring of poly[Ni(OH)$_2$salen] nanoparticle-based electrocatalysts for effective urea remediation†

Monika Mierzejewska, Kamila Łępicka, * Jakub Kalecki and Piyush Sindhu Sharma *

There is no universal recipe for the proper structure tuning of Ni(OH)$_2$ nanoparticle (NP)-based catalysts for efficient urea electrooxidation (UOR) in alkaline media. However, it is known that fast generation of Ni^{3+}OOH-type catalytic centers that are sustained and resilient during the overall catalytic process is crucial. Towards this, we report how we optimized and compared operating conditions and structural tuning of poly[NP-Ni(OH)$_2$SaltMe] and poly[*meso*-NP-Ni(OH)$_2$SaldMe] electrocatalysts active in alkaline media towards UOR. We started with studies of morphological differences evoked by the use of different NaOH$_{aq}$ concentrations for catalyst fabrication by SEM and TEM. Then, we distinguished the most promising molecular structures of fabricated catalysts featuring the highest poisoning resistance and *in situ* generation of poly(NP-Ni^{3+}OOHsalen) electrocatalytic centers for UOR. Furthermore, we found the best conditions for operation of both structured UOR catalysts using a comprehensive electrochemical approach. This approach involved multiple scan rate, Tafel slope, and activation energy (E_{ac}) analysis to finally compare which structured poly[NP-Ni(OH)$_2$salen] catalyst produces catalytic current more efficiently in response to a change in applied potential. Ultimately, we performed a longevity/durability test under real-system mimicking conditions. The fabricated catalysts constituted good platforms for studying the surface-remaining and bulk-remaining types of catalytically active sites of poly[NP-Ni(OH)$_2$salen]s for UOR activity. Our findings point to the bulk-structure-reactivity requirements of poly[NP-Ni(OH)$_2$salen]s, emphasizing their catalytic durability and effectiveness.

Received 24th September 2024,
Accepted 18th December 2024

DOI: 10.1039/d4cy01139b

rsc.li/catalysis

Introduction

Nowadays, there is a need to find an effective method for simultaneous wastewater treatment and electricity generation. The proper treatment of urea-containing wastewater is essential from an energy as well as an environmental point of view. Urea comprises ~45% nitrogen and is a vital crop fertilizer.[1] Part of urea from agricultural fields enters surface water. Another source of urea introduction into the environment is mammalian excretion. The widespread release of non-treated urea-rich wastewater is potentially dangerous for the aquatic system. Moreover, urea pollution triggers sea algae to produce a deadly toxin called domoic acid.[2] The natural decomposition of urea into nitrogen-based pollutants like toxic ammonia harms air quality and eventually causes health risks.[3,4] Using urea-rich wastewater as an alternative energy source has a double benefit. Hence, it can help with wastewater remediation simultaneously with electricity generation.[1,4,5] However, the catalyst cost, efficiency, and problems with scale-up experiments to industrial scale limit the transfer of laboratory experiments to real application.[3,6]

There were many attempts to devise and fabricate heterogeneous electrocatalysts for urea electrooxidation.[1,7,8] Most of them included the involvement of noble metals, such as Pt, Pd, and Rh.[9–13] The high cost, low abundance, and low electrochemical stability limit the commercialization of these noble metal-based catalysts.[14]

Nickel (Ni)-based materials operating in alkaline media are considered the best cost-efficient alternative of catalysts active towards efficient urea electrooxidation.[15–22] The most popular ones are Ni(OH)$_2$-based electrocatalysts, which can oxidize urea in an appropriate alkaline medium concentration to carbon dioxide (in the form of CO_3^{2-}), nitrogen, and water with simultaneous energy release.[23] However, these catalysts still suffer from (i) poor accessibility of active centers in the catalyst bulk and thus slow diffusion of urea[24–26] and (ii) strong adsorption of electrooxidation products to active sites.[27,28] Thus, providing high durability is still one of the challenges restricting Ni(OH)$_2$-based catalysts' large-scale application.

Institute of Physical Chemistry, Polish Academy of Sciences, Kasprzaka 44/52, 01-224 Warsaw, Poland. E-mail: klepicka@ichf.edu.pl, psharma@ichf.edu.pl

† Electronic supplementary information (ESI) available: Additional experimental details, results and supporting tables. See DOI: https://doi.org/10.1039/d4cy01139b

The kinetics of urea oxidation in the absence of a catalyst is slow. On the $Ni(OH)_2$-based electrocatalysts, urea oxidation becomes thermodynamically favourable and can follow the so-called indirect/catalyst regeneration mechanism.[23,29] The indirect/regeneration mechanism involves the electrochemical oxidation of $Ni^{2+}(OH)_2$ to $Ni^{3+}OOH$, following which $Ni^{3+}OOH$ acts as an oxidizer that becomes reduced to $Ni^{2+}(OH)_2$ and oxidizes urea. This regeneration mechanism indicates that urea oxidation proceeds only on OH^- and urea-accessible catalyst centers of $Ni^{3+}OOH$ electrogenerated from $Ni(OH)_2$ forms at thermodynamically favourable potentials in both forward and backward CV scans. However, the balance between OH^- doping ions responsible for active center production in the first step and urea reactant diffusion to those centers must be preserved during the electrocatalytic process. Moreover, based on the indirect/regeneration mechanism, one can deduce the possible adsorption/accumulation of reaction products as well as trapping of OH^- dopant, *i.e.*, the amount of blocked/deactivated $Ni^{3+}OOH$ catalytically active sites. The CV-monitored urea oxidation reveals the formation and stabilization of $Ni^{3+}OOH$ catalytically active sites. The forward scan process of electrocatalytic urea oxidation influences the catalytic peak current height, which appears at a backward scan in the potential range where urea oxidation still proceeds. Therefore, the catalytic performance of $Ni(OH)_2$-based electrocatalysts can be followed and adjusted by comparing forward and backward scan electrocatalytic responses.[30]

The most desired $Ni(OH)_2$-based catalyst operating in alkaline media requires fast charge transfer, causing the generation of $Ni^{3+}OOH$ active centers from $Ni(OH)_2$ pristine forms.[31] Hence, the presence and accessibility of these catalytically active $Ni^{3+}OOH$ forms after OH^- doping, to which urea diffuses as fast as possible, determines its efficiency.[24] By increasing accessibility to the bulk structure of $Ni(OH)_2$-based catalysts for OH^- and urea, one can increase the catalyst activity by increasing the amount of accessible active sites.[3,27,28] Furthermore, a proper concentration of OH^- counterions forcing the change in the binding affinity of urea oxidation products tends to increase their durability.[3,23,27,32,33] However, too high concentrations of OH^- are not preferred from an ecological point of view and may lead to the chemical decomposition of $Ni^{3+}OOH$ active centers,[24,34] according to the Pourbaix diagram. This diagram shows that the $Ni(OH)_2$-based NPs undergo transformation into $HNiO_2$ in a too-high pH.[35] Reported DFT calculations suggested that urea and OH^- when present in the solution compete during diffusion to active centers because of their similar affinity.[33] The OH^- concentration has to be sufficiently high to desorb urea oxidation products from the active sites.[3,32] However, a too high concentration of OH^- in comparison to the concentration of urea can block urea access to active centers .[33,36–38] Therefore, this concentration needs to be optimized to achieve the best operation conditions for the new type of structured $Ni(OH)_2$-based catalyst.

The electrochemical studies performed during the catalytic oxidation of urea on the new Ni^{2+}-based catalysts operating in alkaline media according to the two-step indirect mechanism are aimed at monitoring the impact of urea diffusional limitations.[23,25–27] The electrocatalytic urea oxidation process occurring in the second step on $Ni^{3+}OOH$ centers of properly structured $Ni(OH)_2$-based catalysts is expected to be under urea oxidation control, *i.e.*, under charge transfer control (kinetically controlled). In that case, the slowest step has to be the chemical oxidation of urea on catalytically active centers, not the diffusion of urea to these centers.[1,24,26]

Recently, a few research groups reported the fabrication of $Ni(OH)_2$-type NP electrocatalysts derived from poly[Ni^{2+}(salen)] precursors differing in chemical structure and morphology.[31,39–41] Those $Ni(OH)_2$-type NP catalysts were studied towards electrooxidation of small molecules, *e.g.*, methanol, ethanol, and glycerol.[31,40] The fabrication method of $Ni(OH)_2$-type NPs is called potential-driven generation,[31] and, importantly, it is conducted in a water-based alkaline medium. The uniform distribution of $Ni(OH)_2$-type NPs in the catalyst bulk was preserved by their 3D-templating inside the poly(salen) matrix. Hence, this advantageous arrangement of NPs was found to be dependent on conditions of poly[Ni(salen)] precursor electrodeposition and its molecular structure.[31] However, the effect of alkaline medium concentration on NP fabrication by potential-driven generation still needs to be studied. The $Ni(OH)_2$-type NP catalyst derived from poly[Ni(salen)] precursor electrodeposited under potentiostatic conditions indicated the highest amount of electrocatalytically active centers engaged in ethanol oxidation. Importantly, no active center blocking by ethanol electrooxidation product was observed.[31] In other words, due to the high accessibility of active centers in the catalyst bulk, fast diffusion of ethanol was achieved. Furthermore, we noticed that the use of $Ni(OH)_2$-type NPs embedded in poly(salen) matrixes as a catalyst for urea electrooxidation demands additional structuring and adjusting of catalytic conditions.

Experimental section

Chemicals

Anhydrous acetonitrile (ACN, 99.8%), electrochemical grade tetra(*n*-butyl)ammonium hexafluorophosphate ((TBA)PF_6, ≥99% electrolyte salt), and BioReagent grade urea (NH_2-$CONH_2$, ≥98%) were purchased from Sigma-Aldrich. Analytical grade sodium hydroxide (NaOH) was purchased from POCH. All of these reagents were used without further purification. Carbon paper (CP FuelCellsETc) was purchased from College Station, TX. Two phenyl ring unsubstituted Ni^{2+}-salen monomers differing in the configuration of methyl-substituted imine bridge, (i) the 2,3-dimethyl-*N*,*N*′-bis-(salicylidene)-2,3-butanediaminonickel] (Ni^{2+}SaltMe)[42] and (ii) *meso*-*N*,*N*′-bis(salicylidene)-2,3-butanediaminonickel,[43] were synthesized according to an earlier described methodology

(Scheme 1).[43] Milli-Q water (resistivity 18.2 MΩ cm at 25 °C) was used for measurements in aqueous conditions. Artificial urine containing 0.25 M urea was prepared according to the procedure mentioned by Sarigul *et al.*[44]

Electrochemical cells and apparatus

A BioLogic SP300 potentiostat, controlled by EC-Lab software, coupled with a classical three-electrode glass electrochemical cell, was used for all electrochemical measurements, including poly[Ni(salen)] precursor electrodeposition, potential-driven transformation of these polymer precursors into $Ni(OH)_2$-type NPs embedded in poly(salen) matrixes, and their electrochemical characterization. A 5 mm diameter (~0.196 cm^2 geometrical area) laminated CP electrode,[45] Pt coil, and Ag/Ag^+ pseudoreference (used for experiments performed in organic solvent electrolyte solutions), or Ag/AgCl (3 M KCl) electrode (used for experiments performed under aqueous conditions) served as working, counter, and reference electrodes, respectively.

Electrodeposition of $Ni(OH)_2$-type NP catalyst precursors

The precursor films were deposited by electropolymerization under potentiostatic conditions on a laminated CP electrode from an ACN solution containing 1 mM of Ni^{2+}salen monomer (Ni^{2+}SaltMe or *meso*-Ni^{2+}SaldMe) and 0.1 M (TBA) PF_6. A constant potential of 1.30 V *vs.* Ag/Ag^+ was kept until 130 mC cm^{-2} polymerization charge passed. Consequently, the resulting precursor films were abbreviated as poly(NiSaltMe)$_{130}$ and poly(*meso*-NiSaldMe)$_{130}$.

The conditions of precursor film electrodeposition were adapted based on our previous work, where we observed that poly(*meso*-NiSaldMe) precursor that was potentiostatically electrodeposited by passing 130 mC cm^{-2} was the best performing towards ethanol electrooxidation after its transformation into $Ni(OH)_2$-type NPs.[31]

Optimization of $NaOH_{aq}$ concentration for the potential-driven generation of $Ni(OH)_2$-type NPs

Poly(NiSaltMe)$_{130}$ and poly(*meso*-NiSaldMe)$_{130}$ precursor films were transferred separately to 0.2, 0.5, 1.0, and 2.0 M $NaOH_{aq}$ to fabricate eight different catalysts. These precursor layers were abbreviated as poly[NP-Ni(OH)$_2$SaltMe]$_{0.2\ M}$, poly[NP-Ni(OH)$_2$SaltMe]$_{0.5\ M}$, poly[NP-Ni(OH)$_2$SaltMe]$_{1\ M}$, poly[NP-Ni(OH)$_2$SaltMe]$_{2\ M}$], poly[*meso*-NP-Ni(OH)$_2$SaldMe]$_{0.2\ M}$, poly[*meso*-NP-Ni(OH)$_2$SaldMe]$_{0.5\ M}$, poly[*meso*-NP-Ni(OH)$_2$SaldMe]$_{1\ M}$, and poly[*meso*-NP-Ni(OH)$_2$SaldMe]$_{2\ M}$. The potential-driven precursor transformation into the $Ni(OH)_2$-type NPs was conducted in the potential range of 0.00 to 1.20 V *vs.* Ag/AgCl (3 M KCl) at 20 mV s^{-1} till the Ni^{2+}/Ni^{3+} oxidation and respective reduction current peaks were no longer growing. After NP preparation, electrodes were rinsed with Milli-Q water.

Next, the electrocatalytic responses of fabricated NP catalysts were measured using the same $NaOH_{aq}$ concentration as applied for their potential-driven generation. The appropriate urea volume was added separately or continuously to the electrochemical cell to obtain the following urea concentrations: 0.01, 0.05, 0.1, 0.3, and 0.5 M, and to determine the *in situ* generation ability of active sites and the loss of concentration linearity range.

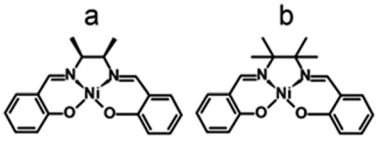

Scheme 1 Structural formulas of (a) *meso*-Ni^{2+}SaldMe and (b) Ni^{2+}SaltMe.

Morphological studies of the $Ni(OH)_2$-type NPs

Poly[NP-Ni(OH)$_2$salen]s fabricated under different $NaOH_{aq}$ concentrations were imaged by scanning electron microscopy (SEM) and transmission electron microscopy (TEM). SEM imaging was performed with an FEI Nova NanoSEM 450 microscope. TEM imaging was carried out using a Talos F200X microscope with Super X energy-dispersive X-ray and an EDX detector. NPs embedded in poly(salen) matrixes were scratched from the CP electrode and placed on a copper grid for TEM imaging.

Optimization of $NaOH_{aq}$ concentration during electrocatalytic oxidation of urea

Poly[NP-Ni(OH)$_2$SaltMe]$_{1\ M}$ and poly[*meso*-NP-Ni(OH)$_2$-SaldMe]$_{1\ M}$, generated in 1.0 M $NaOH_{aq}$, were further examined toward electrooxidation of 0.3 M urea in 0.2, 0.5, 1.0, and 2.0 M $NaOH_{aq}$. The electrocatalytic measurements were carried out in the potential range of 0.00 to 1.00 V *vs.* Ag/AgCl (3 M KCl) at 50 mV s^{-1}. After each catalytic measurement, catalysts were cycled in pure electrolyte solution containing the same concentration of $NaOH_{aq}$ that was used during urea electrooxidation.

Electrocatalytic performance comparison

Multiple scan rate experiments were performed for poly[NP-Ni(OH)$_2$SaltMe]$_{1\ M}$ and poly[*meso*-NP-Ni(OH)$_2$SaldMe]$_{1\ M}$ (i) in 1.0 and 2.0 M $NaOH_{aq}$ (bare electrolyte) and then (ii) in 1.0 M $NaOH_{aq}$ containing 0.3 M urea. These CV responses were registered at the scan rate of 2, 5, 10, 20, 50, 100, and 200 mV s^{-1}. Furthermore, the electron transfer coefficient α and diffusion coefficient D were calculated based on the slope values determined from the peak potential *vs.* the logarithm of the scan rate[46] and the current *vs.* the square root of the scan rate dependencies.

α was calculated according to eqn (1):

$$\alpha = \frac{0.03}{\text{Slope } n_0} \quad (1)$$

where n_0 is the number of electrons exchanged at the interface of the CP electrode|NP-Ni(OH)$_2$salen (Scheme 2). The slope was determined from the linear part of the curve E_{pa} = slope (log ν) + b, where b is the Ni^{2+}/Ni^{3+} oxidation rate constant.

D was calculated according to eqn (2):[47]

$$D = \left(\frac{\text{Slope}}{2.99\times10^5 n((1-\alpha)n_0)^{1/2}AC}\right)^2 \quad (2)$$

where n is the number of electrons involved in urea oxidation (n = 6) at the NP-Ni^{3+}OOH(salen)|solution interface, A is a geometric area of the working electrode (0.196 cm^2), and C is the added urea concentration (0.3 M). The diffusion coefficient of urea in 1.0 M $NaOH_{aq}$ was determined from the linear part of the curve I_{pa} = slope $\nu^{1/2}$.

Linear sweep voltammetry (LSV) curves were measured at 5 mV s^{-1} at the potential range of 0.0 to 1.0 V *vs.* Ag/AgCl (3 M KCl) in a solution containing 0.3 M urea in 1.0 M $NaOH_{aq}$ for poly[NP-Ni(OH)$_2$SaltMe]$_{1\ M}$ and poly[*meso*-NP-Ni(OH)$_2$-SaldMe]$_{1\ M}$. These conditions ensured kinetic control of urea electrooxidation, *i.e.*, the slowest process was urea electrooxidation after its diffusion to accessible catalyst active centers.[48] For these conditions, Tafel slopes for both catalysts were determined from the potential *vs.* the logarithm of the current density, *i.e.*, E *vs.* log(I) plots.

The activation energy (E_{ac}) values were determined for 0.3 M urea electrooxidation in 1.0 M $NaOH_{aq}$ on poly[NP-Ni(OH)$_2$SaltMe]$_{1\ M}$ and poly[*meso*-NP-Ni(OH)$_2$-SaldMe]$_{1\ M}$ at 50 mV s^{-1} in the potential range of 0.0 to 1.0 V *vs.* Ag/AgCl (3 M KCl), measured separately at different temperatures of 16, 19, 24, 28, 33, 38, and 43 °C. The temperature was controlled by two thermocouples placed inside and outside the cell. The E_{ac} values were determined for potentials corresponding to the urea electrooxidation: 0.45 and 0.5 V from the Arrhenius plots. Those plots displayed the current density's logarithm against the temperature's reciprocal, *i.e.*, log(I) *vs.* 1/T. In the absence of urea, the control experiment was prepared under the same conditions.

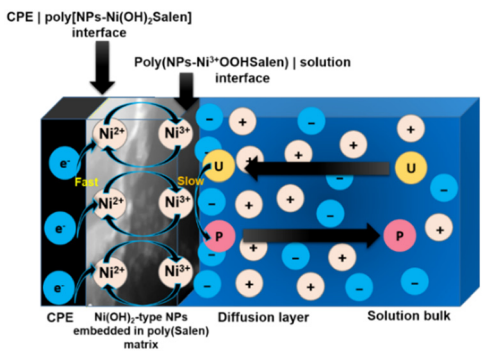

Scheme 2 Illustration of the two-stage catalytic process of urea electrooxidation at the poly[NP-Ni(OH)$_2$salen] catalyst (U: urea, P – product).

Durability test of electrocatalyst in real-system mimicking conditions

To mimic the actual operating conditions of urea fuel cell (UFC) and artificial urine fuel cell (AUFC), a constant potential of 0.55 V *vs.* Ag/AgCl (3 M KCl) was applied to poly[NP-Ni(OH)$_2$SaltMe]$_{1\ M}$ and poly[*meso*-NP-Ni(OH)$_2$-SaldMe]$_{1\ M}$ catalysts for 17 h in 1.0 M $NaOH_{aq}$ in the absence and presence of 0.3 M urea or artificial urine, and the resulting current was recorded.

Results and discussion

Optimization of $NaOH_{aq}$ concentration for potential-driven transformation of poly[Ni(salen)]s

Two phenyl ring unsubstituted Ni^{2+}(salen) complexes, namely Ni^{2+}SaltMe[49] and *meso*-Ni^{2+}SaldMe,[43] differing in methyl substituent configuration on the imine bridge, were deposited on laminated CP electrodes[45] under potentiostatic conditions as poly(Ni^{2+}SaltMe)$_{130}$ (Fig. S1a†) and poly(*meso*-Ni^{2+}SaldMe)$_{130}$ (Fig. S1b†). In this moderately electron-donating medium, Ni^{2+}(salen) monomers electropolymerize in an oxidative manner, forming a conducting film at the electrode surface.[43] These electrodeposited poly[(Ni^{2+}(salen)]s, during the conduction process in moderately electron-donating electrolyte solution, behave like a polyphenylene compound, with the Ni^{2+} acting as a bridge between biphenylene moieties.[50] In such a system, the electron is released from the salen ligand parts.[49–51] However, during the potential-driven transformation of poly[Ni^{2+}(salen)]s into Ni(OH)$_2$-type NPs conducted in a strongly electron-donating medium, *e.g.*, $NaOH_{aq}$, the place of electron release is changed from the salen ligand center to the Ni^{2+}.[31] The formation of Ni(OH)$_2$-type NPs is manifested by a consistent growth of new oxidation and reduction peaks.

During the potential-driven generation process, the poly[Ni^{2+}(salen)] precursors are gradually transformed into Ni(OH)$_2$-type NPs embedded into a non-conducting poly(salen) matrix (Fig. S2 and S3†). The axial coordination of OH^- to the Ni^{2+} centers is crucial for potential-induced cleavage of the bonds between nitrogen belonging to imine moieties and Ni^{2+}, thus resulting in Ni(OH)$_2$-type NP formation inside the poly(salen) polymer matrix. Therefore, one might suppose that an increased $NaOH_{aq}$ concentration would result in faster and more efficient NP generation. However, when we performed NP generation using 0.2, 0.5, 1.0, and 2.0 M $NaOH_{aq}$ by keeping the same scan rate and potential range for poly(NiSaltMe)$_{130}$ and poly(*meso*-NiSaldMe)$_{130}$ precursors deposited in the same manner, we did not observe the time shortening of complete NP generation (Table S1†). However, the highest amount of poly(Ni^{3+}OOHsalen) active centers were generated from both precursors in 1.0 M $NaOH_{aq}$ (Fig. 1a and b, blue curves), indicated by the highest current density. Furthermore, at higher $NaOH_{aq}$ concentrations, the poly[Ni^{2+}(OH)$_2$salen]/poly(Ni^{3+}OOHsalen) electrooxidation and poly(Ni^{3+}OOHsalen)/poly[Ni^{2+}(OH)$_2$salen] electroreduction occurred at lower potential values (Fig. 1a and b). We anticipate that the

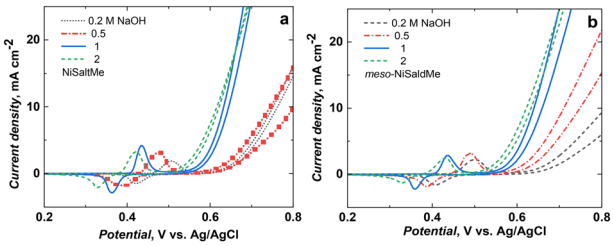

Fig. 1 The last cycle of the potential-driven transformation of (a) poly(NiSaltMe)$_{130}$ and (b) poly(*meso*-NiSaldMe)$_{130}$ into the Ni(OH)$_2$-type NPs, performed at different NaOH$_{aq}$ concentrations.

differences observed in the last CV cycle patterns of the potential-driven transformation of (a) poly(NiSaltMe)$_{130}$ and (b) poly(*meso*-NiSaldMe)$_{130}$ into Ni(OH)$_2$-type NPs, performed in different NaOH$_{aq}$ concentrations are related to potential-induced cleavage of the bonds between nitrogen belonging to imine moieties and Ni^{2+} occurring in bulk and on the surface for poly(*meso*-NiSaldMe)$_{130}$ and poly(NiSaltMe)$_{130}$, respectively.

Morphological characterization of Ni(OH)$_2$-type nanoparticles fabricated at different NaOH$_{aq}$ concentrations

Morphological differences of poly(SaltMe)$_{130}$ and poly(*meso*-SaldMe)$_{130}$ matrixes embedding Ni(OH)$_2$-type NPs evoked by the use of different NaOH$_{aq}$ concentrations in their fabrication process were studied by SEM. This imaging indicated that matrixes of Ni(OH)$_2$-type NPs derived from poly(Ni^{2+}SaltMe)$_{130}$ and poly(*meso*-Ni^{2+}SaldMe)$_{130}$ were differently spatially arranged (Fig. 2). Previously, we observed that the morphology of these poly[Ni^{2+}(salen)] precursors governed by their monomer polymerization conditions and chemical structure influenced the arrangement of Ni(OH)$_2$-type NPs in poly(salen) matrixes when NP-based catalyst fabrication was conducted in 0.2 M NaOH$_{aq}$.[31] Now we have observed that regardless of the NaOH$_{aq}$ concentration used for fabrication, catalysts derived from potentiostatically deposited poly(Ni^{2+}SaltMe)$_{130}$ featured the planar and more condensed arrangement of matrix templating Ni(OH)$_2$-type NPs (Fig. 2a–d). However, the poly(*meso*-SaldMe) matrix arrangement was much more spatially expanded (Fig. 2e–h).

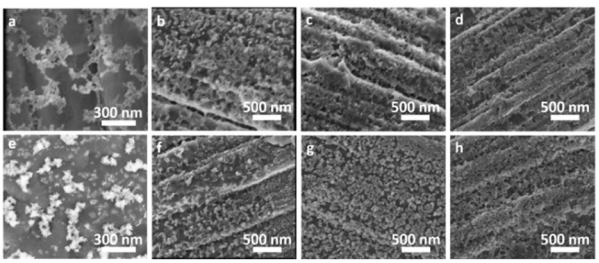

Fig. 2 SEM images of Ni(OH)$_2$-type NPs derived from poly(NiSaldMe)$_{130}$ (a–d) and poly(*meso*-NiSaldMe)$_{130}$ (e–h) fabricated in (a and e) 0.2 M NaOH$_{aq}$, (b and f) 0.5 M NaOH$_{aq}$, (c and g) 1.0 M NaOH$_{aq}$, and (d and h) 2.0 M NaOH$_{aq}$.

As a result of catalyst fabrication from poly(Ni^{2+}SaltMe)$_{130}$ in the low concentrations of NaOH$_{aq}$, carbon fibers were coated with 2D planar poly(SaltMe) matrix templating Ni(OH)$_2$-type NPs (Fig. 2a and b). In high concentrations of NaOH$_{aq}$ (1.0 and 2.0 M), the flake-like 2D poly(SaltMe) matrix covered carbon fibers entirely (Fig. 2c and d). In contrast, the poly(*meso*-SaldMe) matrix resulting from catalyst fabrication in low concentrations of NaOH$_{aq}$ was spatially diversified in 3D and loosely packed (Fig. 2e and f). Fabrication using higher concentrations of NaOH$_{aq}$ caused more uniform coverage of carbon fibers by the poly(*meso*-SaldMe) matrix (Fig. 2g and h). The spacing between neighboring poly(*meso*-SaldMe) matrix parts was significantly bigger when fabrication was conducted in 1.0 M NaOH$_{aq}$ (Fig. 2g).

TEM (Fig. 3 and 4) imaging was used to confirm the presence of nanoscale objects of Ni(OH)$_2$-type NPs embedded in poly(SaltMe) and poly(*meso*-SaldMe) matrixes. The presence of Ni(OH)$_2$-type NPs was additionally confirmed by EDX element mapping (Fig. 3 and 4). Nickel (Ni) and carbon (C) were mapped in red and blue, respectively. The differences in Ni(OH)$_2$-type NP distribution and separation originated from different spatial arrangements of poly(SaltMe) and poly(*meso*-SaldMe) matrixes as indicated by SEM.

The size of NPs in the poly(SaltMe) matrix was below 5 nm (Fig. 3a, a′ and a″). However, a false impression of NPs aggregates was visible when two matrix fragments

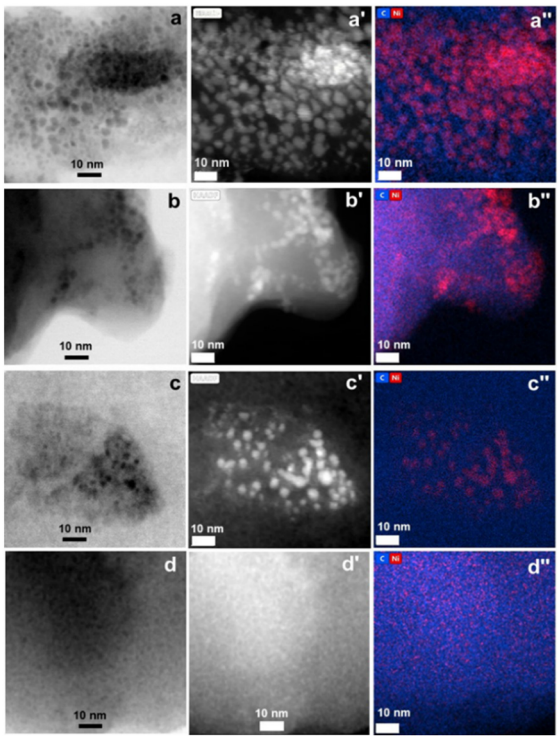

Fig. 3 TEM (a–d), HAADF images (a′–d′) and corresponding EDX mapping (a″–d″) of Ni(OH)$_2$-type NPs derived from poly(NiSaltMe)-PS$_{130}$ in various NaOH$_{aq}$ concentrations. (a) 0.2 M, (b) 0.5 M, (c) 1.0 M, and (d) 2.0 M. EDX profiles for Ni (red) and carbon (blue).

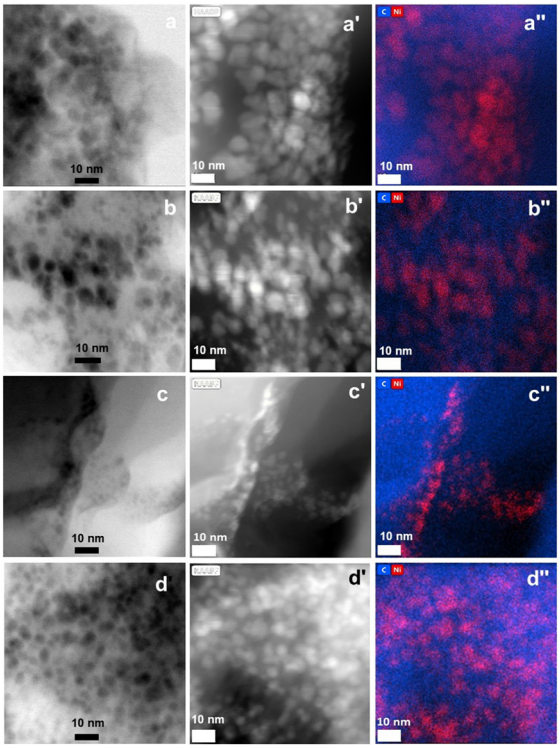

Fig. 4 TEM (a–d), HAADF images (a′–d′) and corresponding EDX mapping (a″–d″) of Ni(OH)$_2$-type NPs derived from poly(*meso*-NiSaldMe)-PS$_{130}$ in various NaOH$_{aq}$ concentrations. (a) 0.2 M, (b) 0.5 M, (c) 1.0 M, and (d) 2.0 M. EDX profiles for Ni (red) and carbon (blue).

overlapped, as visible on the TEM images (Fig. 3a, a′ and a″). Sizes of NPs generated in 0.5 M (Fig. 3b, b′ and b″) and 1.0 M NaOH$_{aq}$ (Fig. 3c, c′ and c″) were slightly smaller than NPs generated in 0.2 M NaOH$_{aq}$ (Fig. 3a, a′ and a″), while the size of NPs was substantially lower (below 2 nm) in the catalyst generated in 2.0 M NaOH$_{aq}$ (Fig. 3d, d′ and d″). This suggested that NPs generated from poly(NiSaltMe) at such high NaOH$_{aq}$ were chemically not stable.

Opposite to this, Ni(OH)$_2$-type NPs generated from poly(*meso*-Ni^{2+}SaldMe)$_{130}$, in different NaOH$_{aq}$ solutions had different sizes. NPs generated from a lower concentration of NaOH$_{aq}$ (0.2 and 0.5 M NaOH$_{aq}$) were slightly bigger in size than NPs generated in a higher concentration of NaOH$_{aq}$ (Fig. 4). More importantly, the size of NPs generated from poly(*meso*-Ni^{2+}SaldMe), in different concentrations of NaOH$_{aq}$, were higher than the size of NPs generated from poly(Ni^{2+}SaltMe). Even at 2.0 M NaOH$_{aq}$ concentration, NPs were visible (Fig. 4). It appears that NP embedment in poly(salen) matrixes allowed stabilizing Ni(OH)$_2$ subnanoclusters down to the nanometer.

The preliminary understanding of the electrocatalytic performance of Ni(OH)$_2$-type NPs fabricated under different alkaline medium concentrations towards urea oxidation

The electrocatalytic responses of poly[NP-Ni(OH)$_2$SaltMe]$_{0.2\ M}$, poly[NP-Ni(OH)$_2$SaltMe]$_{0.5\ M}$, poly[NP-Ni(OH)$_2$SaltMe]$_{1\ M}$, poly[NP-Ni(OH)$_2$SaltMe]$_{2\ M}$, poly[*meso*-NP-Ni(OH)$_2$SaldMe]$_{0.2\ M}$, poly[*meso*-NP-Ni(OH)$_2$SaldMe]$_{0.5\ M}$, poly[*meso*-NP-Ni(OH)$_2$SaldMe]$_{1\ M}$, and poly[*meso*-NP-Ni(OH)$_2$SaldMe]$_{2\ M}$ were registered in the solutions containing the same concentration of NaOH$_{aq}$ as that used for their potential-driven generation. To these solutions, urea portions were added separately (Fig. 5a–d and 6a–d) or continuously (Fig. S4a–d and S5a–d†) to obtain final urea concentrations of 0.01, 0.05, 0.1, 0.3, and 0.5 M. However, during continuous addition, urea is consumed during electrooxidation, resulting in a final concentration that is not as intended. Moreover, continuous urea addition leads to the accumulation of electrooxidation products in the system. In contrast, there is no continuous accumulation of reaction products when urea portions are added separately. Hence, the final concentration added is as intended. The comparison of results obtained after these two different urea addition ways can indicate which of the studied catalysts is more resistant to the presence of oxidation products in the electrocatalytic system and poisoning.

The preparation of the above experiments aimed at a preliminary understanding of the electrocatalytic mechanism of urea electrooxidation in alkaline media on the Ni(OH)$_2$-type NPs embedded in poly(SaltMe) and poly(*meso*-SaldMe) matrixes fabricated in different concentrations of NaOH$_{aq}$. This step is crucial for further identifying the best fabrication conditions of poly[NP-Ni(OH)$_2$salen] catalysts. Above all, it directs the further optimization of the best conditions of urea electrooxidation on our structured catalysts.

In the absence of urea, all of the Ni(OH)$_2$-type NP-based catalysts fabricated in different concentrations of NaOH$_{aq}$ exhibited a typical Ni^{2+}/Ni^{3+} [31,40] electrooxidation peak of poly[Ni^{2+}(OH)$_2$salen]/poly(Ni^{3+}OOHsalen) in the forward scan and its respective poly(Ni^{3+}OOHsalen)/poly[Ni^{2+}(OH)$_2$salen] reduction peak in the backward scan (Fig. 5, 6, S4 and S5,† black curves). Furthermore, at higher NaOH$_{aq}$

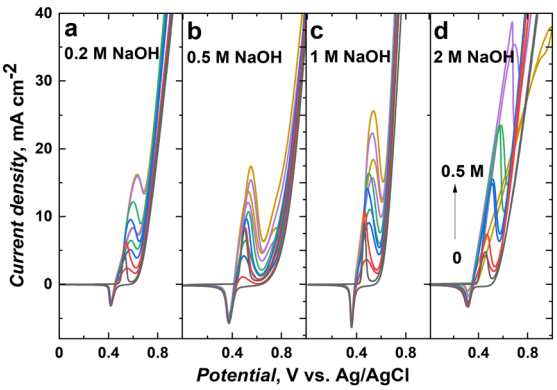

Fig. 5 The electrocatalytic CV responses of Ni(OH)$_2$-type NPs fabricated at (a) 0.2 M, (b) 0.5 M, (c) 1.0 M and (d) 2.0 M NaOH$_{aq}$ from poly(NiSaltMe)$_{130}$ towards the electrooxidation of 0.01, 0.05, 0.1, 0.2, and 0.5 M urea. Urea portions were added separately to the cell to reach the final concentration values. The electrocatalytic CV responses were performed at 50 mV s^{-1} in the solution containing (a) 0.2 M, (b) 0.5 M, (c) 1.0 M, and (d) 2.0 M NaOH$_{aq}$.

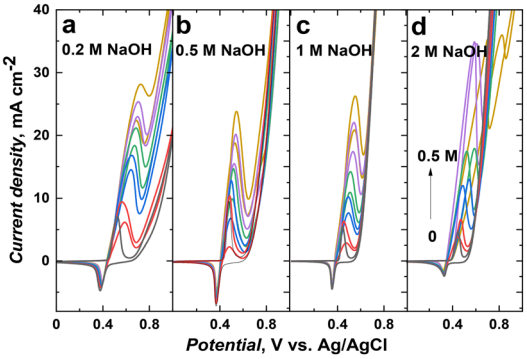

Fig. 6 The electrocatalytic CV responses of $Ni(OH)_2$-type NPs fabricated at (a) 0.2 M, (b) 0.5 M, (c) 1.0 M and (d) 2.0 M $NaOH_{aq}$ from poly(*meso*-NiSaldMe)$_{130}$ towards the electrooxidation of 0.01, 0.05, 0.1, 0.2, and 0.5 M urea. Urea portions were added separately to the cell to reach the final concentration values. The electrocatalytic CV responses were performed at 50 mV s^{-1} in the solution containing (a) 0.2 M, (b) 0.5 M, (c) 1.0 M, and (d) 2.0 M $NaOH_{aq}$.

concentrations, the electrooxidation processes of Ni^{2+}/Ni^{3+} electrooxidation and Ni^{3+}/Ni^{2+} electroreduction occurred at lower potentials (Fig. 5, 6, S4, and S5,† black curves). At potentials exceeding ~0.75 V, the forward anodic current increased further because of the oxygen evolution reaction (OER).[52]

After urea additions, all of the studied poly[NP-Ni$(OH)_2$-salen] catalysts followed the so-called indirect mechanism[28,29,38] of urea oxidation. This mechanism is indirect because urea oxidation occurs only at accessible and catalytically active poly(NP-Ni^{3+}OOHsalen) centers. Gradually electrogenerated poly(NP-Ni^{3+}OOHsalen) centers mediate the chemical oxidation of urea to CO_2 (in the form CO_3^{2-}) and N_2 [3,38] (eqn (4)) with simultaneous reduction of poly(NP-Ni^{3+}-OOHsalen) centers to poly[NP-$Ni^{2+}(OH)_2$salen] in between forward and backward scan, defined as 'catalyst regeneration'. What is important is that this 'catalyst regeneration' to poly[NP-$Ni^{2+}(OH)_2$salen] can decrease the amount of poly(NP-Ni^{3+}OOHsalen) catalytically active sites during the overall process.

Analyzing electrocatalytic CV responses registered for separately added urea (Fig. 5 and 6), it is visible that the current increases in the forward scan until the number of poly(NP-Ni^{3+}OOHsalen) accessible active sites is not reduced to poly[NP-$Ni^{2+}(OH)_2$salen] by chemical oxidation of urea. This results in a current density decrease after the peak when products are formed. The second peak of urea oxidation on accessible poly(NP-Ni^{3+}OOHsalen) centers increases in the backward scan at the potentials where urea can be electrooxidized. The higher the backward peak, the better the electrocatalytic performance due to the greater durability and availability of poly(NP-Ni^{3+}OOHsalen) centers.

$$6\ \text{poly[NPs-Ni}^{2+}\text{(OH)}_2\text{Salen]} + 6\ OH^- \rightleftharpoons 6\ \text{poly(NPs-Ni}^{3+}\text{OOHSalen)} + 6\ H_2O + 6\ e^- \quad (3)$$

Catalyst regeneration

$$6\ \text{poly(NPs-Ni}^{3+}\text{OOHSalen)} + CO(NH_2)_2 + H_2O \rightarrow 6\ \text{poly[NPs-Ni}^{2+}\text{(OH)}_2\text{Salen]} + N_2 + CO_2 \quad (4)$$

In situ generation/retention ability of poly(NP-Ni^{3+}OOHsalen) centers

According to the identified indirect mechanism of urea electrooxidation on poly[NP-Ni$(OH)_2$salen], the amount of charge corresponding to urea electrooxidation on accessible poly(NP-Ni^{3+}OOHsalen) centers in the forward scan (Q_1) is equal to the integrated area under the $I(t)$ curve. Meanwhile, Q_2 integrated from the $I(t)$ in the backward scan is the amount of charge associated with urea oxidation on poly(NP-Ni^{3+}OOHsalen) centers that remain accessible after a chemical reaction. Knowing the values of Q_1 and Q_2, we calculated the percentage of active centers that were still accessible for urea electrooxidation in the backward scan. In this way, the *in situ* generation abilities of catalytically active centers for differently structured poly[NP-Ni$(OH)_2$salen] catalysts in the presence of different concentrations of urea added either separately or continuously were compared.

We did not observe common systematic relations in the generation of active centers on poly[NP-Ni$(OH)_2$SaltMe]$_{0.2\ M}$ and poly[*meso*-NP-Ni$(OH)_2$SaldMe]$_{0.2\ M}$ in 0.2 M $NaOH_{aq}$ during continuous or separate addition of increased concentrations of urea (Table S2†). In the presence of 0.3 M urea in 0.2 M $NaOH_{aq}$, poly[*meso*-NP-Ni$(OH)_2$SaldMe]$_{0.2\ M}$ catalyst, *in situ* generation ability was higher in comparison to other concentrations of urea (Table S2†). The % Q_s and % Q_c were 84.7% and 69.9% for separately and continuously added urea, respectively. We noticed much lower *in situ* generation abilities (45–55%) for poly[NP-Ni$(OH)_2$SaltMe]$_{0.2\ M}$ operating in 0.2 M $NaOH_{aq}$ for all added urea. In 0.5 M $NaOH_{aq}$ with the increasing additions of urea for poly[NP-Ni$(OH)_2$SaltMe]$_{0.5\ M}$ and poly[*meso*-NP-Ni$(OH)_2$SaldMe]$_{0.5\ M}$, the *in situ* generation ability increased regardless of whether urea was added separately or continuously (Fig. 5b, 6b, S4b, and S5b and Table S3†). Meanwhile, for separately added urea portions exceeding 0.3 M, added to 1.0 M $NaOH_{aq}$, for poly[*meso*-NP-Ni$(OH)_2$SaldMe]$_{1\ M}$ and poly[NP-Ni$(OH)_2$-SaltMe]$_{1\ M}$, *in situ* generation abilities were 83.9–84.6% and 80.3–81.7%, respectively (Table S4†). The higher *in situ* generation ability observed for poly[*meso*-NP-Ni$(OH)_2$SaldMe]$_{1\ M}$ indicated that this catalyst retained more active sites during the backward scan. *In situ* generation abilities for continuous urea additions after reaching 0.3 M were 83.5% and 75.1% for poly[*meso*-NP-Ni$(OH)_2$SaldMe]$_{1\ M}$, and poly[NP-Ni$(OH)_2$SaltMe]$_{1\ M}$, respectively. This showed a significant effect of the electrooxidation product accumulation in the poly[NP-Ni$(OH)_2$SaltMe]$_{1\ M}$ catalyst.

The smaller differences in Q% values obtained for poly[*meso*-NP-Ni$(OH)_2$SaldMe]$_{1\ M}$, regardless of whether urea was added separately or continuously indicated that this catalyst is resistant to the presence of catalytic reaction products. Consequently, oxidation products are more effectively desorbing from the poly(*meso*-NP-Ni^{3+}OOHSaldMe)$_{1\ M}$ active sites than from poly(NP-Ni^{3+}OOHSaltMe)$_{1\ M}$ centers.

Forward scan electrocatalytic peak currents of poly[NP-Ni$(OH)_2$SaltMe]$_{2\ M}$ and poly[*meso*-NP-Ni$(OH)_2$SaldMe]$_{2\ M}$ were

shifting towards higher potential values in 2.0 M $NaOH_{aq}$ (Fig. 5d, 6d, S4d and S5d†). This behavior can be attributed to poly(NP-Ni^{3+}OOHsalen) active center blocking by OH^- ions when considering separate urea additions (Fig. 5d and 6d). Under these conditions, OH^- ions and urea molecules compete to access active centers. However, when urea was added continuously, the potential shift in 2 M $NaOH_{aq}$ was more prominent (Fig. S4d and S5d†). Thus, this points to gradual active center blocking by the accumulation of reaction products that was most probably coupled with the influence of too-high concentrations of OH^- ions. Additionally, it suggests electrocatalyst chemical stability issues in 2.0 M $NaOH_{aq}$. This can be explained with the use of the potential/pH diagram. At 2.0 M $NaOH_{aq}$, the $Ni(OH)_2$-type NPs start to be chemically unstable and probably convert to $HNiO_2^-$ according to eqn (5):[35]

$$Ni(OH)_2 + OH^- \rightleftharpoons HNiO_2^- + H_2O \quad (5)$$

Moreover, for poly[NP-$Ni(OH)_2$SaltMe]$_{2\ M}$ electrocatalytic responses register during separate (Fig. 5d) and continuous urea additions (Fig. S4d†), generation ability could not be determined because of overlapping of urea oxidation and OER processes.

The best results were obtained for both catalysts fabricated in 1.0 M $NaOH_{aq}$. These catalysts indicated the highest ability of active center generation in 1.0 M $NaOH_{aq}$ (Table S4†). Furthermore, the higher *in situ* generation abilities obtained for poly[*meso*-NP-$Ni(OH)_2$SaldMe]$_{1\ M}$ revealed that this catalyst is more resistant to the presence of electrooxidation products.

Knowing that increasing the urea concentration increases the anodic peak current density if the catalytic reaction is under diffusion control,[23] we analyzed the electrocatalytic responses of poly[NP-$Ni(OH)_2$salen] catalysts fabricated in different $NaOH_{aq}$ concentrations, focusing on the linearity ranges obtained after the separate urea additions (Fig. 5 and 6). For all poly[NP-$Ni(OH)_2$salen] catalysts fabricated in different $NaOH_{aq}$ concentrations, forward scan peak current density increase was observed after separate urea additions until 0.3 M (Fig. 5 and 6). This observation is connected with competing interactions of urea with OH^- counterions to reach the accessible active centers. When the urea concentration was too low to overcome this competition, the diffusion of urea molecules to the accessible active sites was the slowest process. However, for urea concentrations greater than 0.3 M (Fig. 5 and 6), the amount of urea was sufficient to overcome the binding affinity competition with OH^-, and the urea electrooxidation on the poly(NP-Ni^{3+}OOHsalen) active sites became the slowest step. Because of that, for further experiments, we chose a urea concentration of 0.3 M.

Optimization of $NaOH_{aq}$ concentration during electrocatalytic oxidation of urea on structurally tuned catalysts

The onset potential is one of the most important parameters describing the studied material's electrocatalytic performance. It is defined as the lowest potential value at which the reaction products start to appear.[53,54] A simultaneous decrease in the onset potential and increased anodic peak current density in the forward scan indicate higher catalytic activity for urea electrooxidation catalysts operating in alkaline electrolytes.[3] Consecutively, the higher backward anodic peak current density indicates higher resistance against poisoning/product accumulation according to the indirect mechanism.[23,29] Additionally, it was shown that an increase in an alkaline electrolyte concentration may result in shifting the onset potential to lower values and increasing the anodic peak current density, thus forcing oxidation of intermediates and desorption of final reaction products.[32] Encouraged by these facts, two NP catalysts, poly[NP-$Ni(OH)_2$SaltMe]$_{1\ M}$ and poly[*meso*-NP-$Ni(OH)_2$-SaldMe]$_{1\ M}$, fabricated in 1.0 M $NaOH_{aq}$, revealing the best *in situ* generation ability, were chosen to optimize the best $NaOH_{aq}$ concentration for the electrocatalytic oxidation of 0.3 M urea. Both catalysts were electrochemically examined in the absence (Fig. S6†) and presence of 0.3 M urea (Fig. 7) in 0.2, 0.5, 1.0, and 2.0 M $NaOH_{aq}$.

In the urea-free electrolyte solution, a shift of Ni^{2+}/Ni^{3+} oxidation/reduction potentials to lower values was observed with increasing $NaOH_{aq}$ concentration (Fig. S6a and b†). Moreover, there were visible differences in the peak current heights. The highest current density was obtained for CV responses registered in 1.0 and 0.5 M $NaOH_{aq}$ for poly[NP-$Ni(OH)_2$SaltMe]$_{1\ M}$ (Fig. S6,† red and blue curves) and for 1.0 M $NaOH_{aq}$ for poly[*meso*-NP-$Ni(OH)_2$SaldMe]$_{1\ M}$ (Fig. S6b,† red curve), indicating that the highest amount of poly(NP-Ni^{3+}OOHsalen) active centers was electrogenerated for those $NaOH_{aq}$ concentrations. Furthermore, slightly higher current density obtained for poly[*meso*-NP-$Ni(OH)_2$SaldMe]$_{1\ M}$ indicated that more active sites were electrogenerated for this catalyst. The lower current density observed in the presence of 2.0 M $NaOH_{aq}$ suggested that in this concentration, both catalysts might be chemically unstable and side reactions occur (the example of such a side reaction is presented in eqn (5)).

In the presence of urea (Fig. 7), a shift in the onset potential of the urea electrooxidation to lower values was

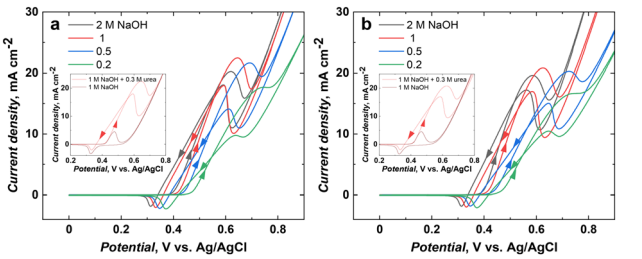

Fig. 7 The catalytic CV responses of (a) poly[NP-$Ni(OH)_2$SaltMe]$_{1\ M}$, and (b) poly[*meso*-NP-$Ni(OH)_2$ SaldMe]$_{1\ M}$ toward 0.3 M urea in different NaOHaq concentrations. The CVs were performed at 50 mV s^{-1}. Insets display CV responses of (a) poly[NP-$Ni(OH)_2$SaltMe]$_{1\ M}$, and (b) poly[*meso*-NP-$Ni(OH)_2$SaldMe]$_{1\ M}$ registered at 50 mV s^{-1} in the presence and absence of 0.3 M urea in 1.0 M $NaOH_{aq}$.

observed with the increase of the $NaOH_{aq}$ concentration for both poly[NP-Ni(OH)$_2$salen]$_{1\ M}$ structured catalysts. Comparing these two catalysts, lower onset potential values were obtained for poly[*meso*-NP-Ni(OH)$_2$SaldMe]$_{1\ M}$ when comparing 0.3 M urea electrooxidation for all $NaOH_{aq}$ concentrations (Table 1). Most likely, it is because of the more efficient generation of poly(*meso*-NP-Ni^{3+}OOHSaldMe) catalytically active centers and their bigger spatial accessibility for urea and OH^-. This accessibility seemed disrupted when catalytic oxidation was conducted in 2.0 M $NaOH_{aq}$ (Fig. 7a and b, black curves). Hence, it is directly reflected in the lack of simultaneous anodic peak growth and onset potential decrease because of too strong adsorption of OH^- resulting in the merging of the OER[55] with urea oxidation in 2.0 M $NaOH_{aq}$. These results revealed that 2.0 M $NaOH_{aq}$ was not appropriate for urea oxidation on poly[NP-Ni(OH)$_2$SaltMe]$_{1\ M}$ and poly[*meso*-NP-Ni(OH)$_2$SaldMe]$_{1\ M}$. The origin and comparison of the impact of active center blocking in 2.0 M $NaOH_{aq}$ for structured catalysts is described in detail in the part describing multiple scan rate experiments conducted in blank $NaOH_{aq}$.

Electrocatalytic performance comparison of poly[NP-Ni(OH)$_2$SaltMe]$_{1\ M}$ and poly[*meso*-NP-Ni(OH)$_2$SaldMe]$_{1\ M}$

Multiple scan rate experiments were registered for poly[NP-Ni(OH)$_2$SaltMe]$_{1\ M}$ and poly[*meso*-NP-Ni(OH)$_2$SaldMe]$_{1\ M}$ in two different concentrations of pure electrolyte: 1.0 M $NaOH_{aq}$ (Fig. 8 and 9) and 2.0 M $NaOH_{aq}$ (Fig. S7 and S8†). These experiments aimed to determine differences in the limiting conditions of the electrochemical redox process of poly[NP-Ni^{2+}(OH)$_2$salen] ⇌ poly[NP-Ni^{3+}OOHsalen] influenced by the electrochemical dopant concentration for both differently structured materials.

Multiple scan rate CV responses registered for poly[NP-Ni(OH)$_2$SaltMe]$_{1\ M}$ and poly[*meso*-NP-Ni(OH)$_2$SaldMe]$_{1\ M}$ in 1.0 M $NaOH_{aq}$ (Fig. 8 and 9) and 2.0 M $NaOH_{aq}$ (Fig. S7a and S8a†) revealed that the characteristic peak currents corresponding to electrooxidation and electroreduction of nickel hydroxide-type redox centers, poly[NP-Ni^{2+}(OH)$_2$salen] ⇌ poly[NP-Ni^{3+}OOHsalen], were linearly dependent on the scan rate up to 20 mV s^{-1} (Fig. 8b, 9b, S7b and S8b), indicating that considered electrochemical redox processes occurring in 1.0 M and 2.0 M $NaOH_{aq}$ for both materials were under finite diffusion control[56] of charge maintaining OH^- counterions. However, at scan rates above 20 mV s^{-1}, it seems

Table 1 Onset potential measured in different concentrations of $NaOH_{aq}$ in the presence of 0.3 M urea for poly[NP-Ni(OH)$_2$SaltMe]$_{1\ M}$ and poly[*meso*-NP-Ni(OH)$_2$SaldMe]$_{1\ M}$

C_{NaOH} (M)	Poly[NP-Ni(OH)$_2$SaltMe]$_{1\ M}$ onset potential (V)	Poly[*meso*-NP-Ni(OH)$_2$SaldMe]$_{1\ M}$ onset potential (V)
0.2	0.474	0.466
0.5	0.445	0.438
1.0	0.424	0.416
2.0	0.406	0.399

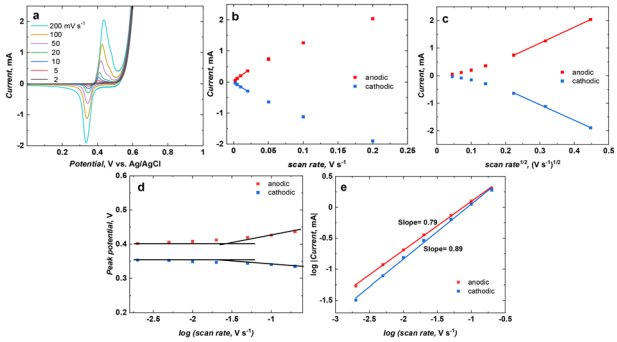

Fig. 8 (a) CV curves measured over poly[NP-Ni(OH)$_2$SaltMe]$_{1\ M}$ at 2, 5, 10, 30, 50, 100, 200 mV s^{-1} scan rate in 1.0 M $NaOH_{aq}$. (b) The anodic (red curve) and cathodic (blue curve) peak current dependence on the scan rate. (c) The anodic and cathodic peak currents *vs.* the square root of the scan rate. (d) The anodic and cathodic peak potentials *vs.* the logarithm of the scan rate. (e) The logarithm of the anodic and cathodic peak currents *vs.* the logarithm of the scan rate.

that the characteristic peak currents (Fig. 8c, 9c, S7c, and S8c†) were linearly dependent on the square root of scan rates, thus suggesting that diffusion of OH^- was close to entering a semi-infinitive diffusion regime[48] in 1.0 M and 2.0 M $NaOH_{aq}$ for both materials.

Comparing multiple scan rate responses within one material, *i.e.*, separately poly[NP-Ni(OH)$_2$SaltMe]$_{1\ M}$ and poly[*meso*-NP-Ni(OH)$_2$SaldMe]$_{1\ M}$, operating either in 1.0 M or in 2.0 M $NaOH_{aq}$ one can notice the differences in the current level and reversibility of the redox processes. Higher current levels coupled with the Nernstian nature of electrochemical responses were observed in 1.0 M $NaOH_{aq}$ for both analyzed materials. Hence, the peak potential separation observed for poly[NP-Ni(OH)$_2$SaltMe]$_{1\ M}$ (Fig. 8d) and poly[*meso*-NP-Ni(OH)$_2$SaldMe]$_{1\ M}$ (Fig. 9d) in 1.0 M $NaOH_{aq}$ was low, up to 20 mV s^{-1}, and then it increased because the OH^- diffusion cannot keep the rate of charge transfer. The lower current level responses (Fig. S7a and

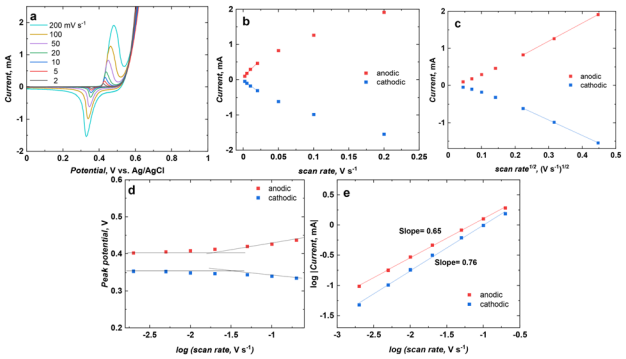

Fig. 9 (a) CV curves of poly[*meso*-NP-Ni(OH)$_2$SaldMe]$_{1\ M}$ at 2, 5, 10, 30, 50, 100, and 200 mV s^{-1} scan rate in 1.0 M $NaOH_{aq}$. (b) The anodic (red curve) and cathodic (blue curve) peak current dependence on the scan rate. (c) The anodic and cathodic peak currents *vs.* the square root of the scan rate. (d) The anodic and cathodic peak potentials *vs.* the logarithm of the scan rate. (e) The logarithm of the anodic and cathodic peak currents *vs.* the logarithm of the scan rate.

S8a†), increased peak potential separations (Fig. S7d and S8d†), and lower values of the slopes determined from the dependence of the logarithm of the peak currents *vs.* the logarithm of the scan rate observed for both materials operating in 2.0 M $NaOH_{aq}$ pointed out hindered OH^- diffusion to redox centers. This suggests that redox centers of both materials, poly[NP-Ni$(OH)_2$SaltMe]$_{1\ M}$ and poly[*meso*-NP-Ni$(OH)_2$SaldMe]$_{1\ M}$, operating in 2.0 M $NaOH_{aq}$ were blocked by too strong adsorption of counterions that most probably resulted in chemical degradation of centers.

Meanwhile, the differences between the Nernstian multiple scan rate responses registered in 1.0 M $NaOH_{aq}$ for poly[NP-Ni$(OH)_2$SaltMe]$_{1\ M}$ and poly[*meso*-NP-Ni$(OH)_2$SaldMe]$_{1\ M}$ are indicative of the nature of the OH^- finite diffusion control electrochemical redox process. The slope value determined from the dependence of the logarithm of the peak currents *vs.* the logarithm of the scan rate for poly[NP-Ni$(OH)_2$SaltMe]$_{1\ M}$ was 0.79 (Fig. 8e), which is characteristic of an electrochemical redox process occurring on the surface of the active material,[57] while the lower slope value (0.65) obtained for poly[*meso*-NP-Ni$(OH)_2$SaldMe]$_{1\ M}$ (Fig. 9e) indicates that the fast electrochemical redox process occurred in the bulk of the active material. This signifies that the poly(SaltMe) matrix is relatively flat and possesses active sites close to the surface. In contrast, the poly(*meso*-SaldMe) matrix is spatially diversified, and Ni^{3+}OOH active sites are embedded in the bulk of the matrix.

The multiple scan rate electrocatalytic responses of the poly[NP-Ni$(OH)_2$SaltMe]$_{1\ M}$ and poly[*meso*-NP-Ni$(OH)_2$SaldMe]$_{1\ M}$ catalysts were registered in 1.0 M $NaOH_{aq}$ solution containing 0.3 M urea to distinguish which of these two structured catalyst indicated better catalytic performance. To obtain the origin of the differences in the electrocatalytic oxidation of urea on the poly[NP-Ni$(OH)_2$SaltMe]$_{1\ M}$ and poly[*meso*-NP-Ni$(OH)_2$SaldMe]$_{1\ M}$ at different scan rates, we coupled previously obtained conclusions considering active center generation in pure 1.0 M $NaOH_{aq}$ with new findings from electrocatalytic oxidation of urea experiments probing its active center accessibility.

The electrochemical responses obtained for both catalysts in the presence of 0.3 M urea did not show the electrocatalytic peak current heights remaining at the same level for all studied scan rates (Fig. 10a and 11a). Fig. 10b and 11b show that the peak currents were linearly dependent on the square root of the scan rate below 20 mV s^{-1}, thus indicating that only for those scan rates the desired charge transfer control of urea oxidation on fast generated poly[NP-Ni^{3+}OOHsalen] was achieved. Above 20 mV s^{-1}, the generation of active centers was slow, thus reflecting OH^--diffusion limitations recognized in the experiment conducted in 1.0 M $NaOH_{aq}$ (Fig. 8 and 9). Additionally, the dependence of catalytic peak currents normalized towards the square root of the scan rate plotted *vs.* scan rate confirmed that the desired chemical oxidation of urea was the controlling step, *i.e.*, the slowest step of the overall electrocatalytic process occurring below 20 mV s^{-1} (Fig. 10e and 11e). At scan rates

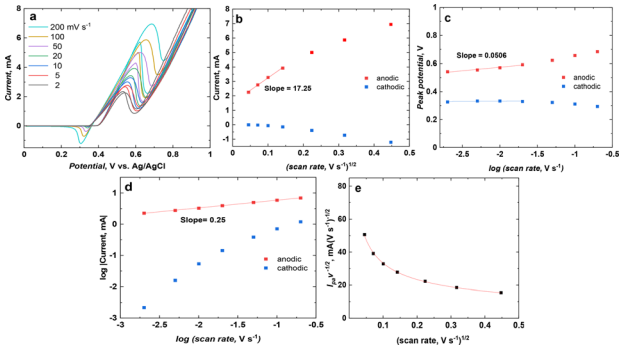

Fig. 10 (a) CV curves of poly[NP-Ni$(OH)_2$SaltMe]$_{1\ M}$ at 2, 5, 10, 20, 50, 100, 200 mV s^{-1} scan rate in the presence of 0.3 M urea in 1.0 M $NaOH_{aq}$. (b) The anodic and cathodic peak currents *vs.* the square root of the scan rate. (c) The anodic and cathodic peak potentials *vs.* the logarithm of the scan rate. (d) The logarithm of the anodic and cathodic peak currents *vs.* the logarithm of the scan rate. (e) The scan rate normalized current ($I_{pa}\ v^{-1/2}$) *vs.* the square root of the scan rate.

higher than 20 mV s^{-1}, the generation of poly[NP-Ni^{3+}-OOHsalen] forms was slowed down because of OH^- diffusional limitations; thus, the normalized current values on Fig. 10e and 11e did not change much. Moreover, the slope of the logarithm of the current *vs.* the logarithm of the scan rate determined for 2 to 20 mV s^{-1} was 0.25 (Fig. 10d) and 0.24 (Fig. 11d) for poly[NP-Ni$(OH)_2$SaltMe]$_{1\ M}$ and poly[*meso*-NP-Ni$(OH)_2$SaldMe]$_{1\ M}$, respectively, indicating that the accessibility of the poly[*meso*-NP-Ni^{3+}OOHSaldMe] electrocatalytically active sites for urea was bigger.

Furthermore, to parameterize the poly[NP-Ni$(OH)_2$SaltMe]$_{1\ M}$ and poly[*meso*-NP-Ni$(OH)_2$SaldMe]$_{1\ M}$ molecular structure differences and their implication for the electrocatalytic urea oxidation process, α and D were calculated based on data obtained from the electrocatalytic multiple scan rate experiment. These parameters are related to the electrocatalytic process occurring at the interface of the NP-Ni^{3+}OOHsalen|urea containing solution – 2nd interface

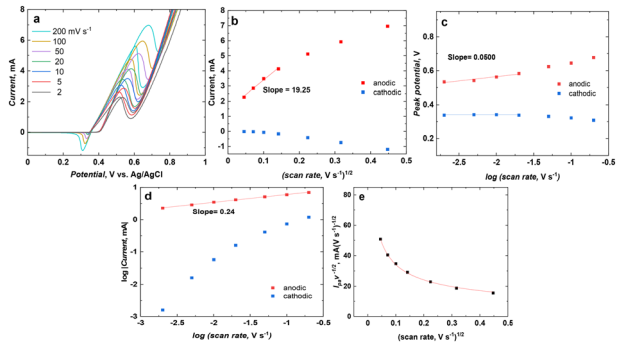

Fig. 11 (a) CV curves of poly[*meso*-NP-Ni$(OH)_2$SaldMe]$_{1\ M}$ at 2, 5, 10, 20, 50, 100, 200 mV s^{-1} scan rates in the presence of 0.3 M urea in 1.0 M $NaOH_{aq}$. (b) The anodic and cathodic peak currents *vs.* the square root of the scan rate. (c) The anodic and cathodic peak potentials *vs.* the logarithm of the scan rate. (d) The logarithm of the anodic and cathodic peak currents *vs.* the logarithm of the scan rate. (e) The scan rate normalized current ($I_{pa}\ v^{-1/2}$) *vs.* the square root of the scan rate.

(Scheme 2). α is associated with the electrocatalytic charge transfer occurring at the NP-Ni^{3+}OOHsalen|urea interface, *i.e.*, the second interface (Scheme 2). α can range from 0 to 1; α <0.5 means a one-electron process, and α >0.5 indicates a multistep system. The α values were calculated according to eqn (1) based on the slopes determined for data obtained in the scan rate range of 2 to 20 mV s^{-1} (Fig. 10c and 11c). The α values were 0.59 and 0.60 for poly[NP-Ni(OH)$_2$SaltMe]$_{1\ M}$ and poly[*meso*-NP-Ni(OH)$_2$SaldMe]$_{1\ M}$ catalysts, respectively. These values confirmed that urea undergoes oxidation according to the two-step indirect mechanism where six electrons are exchanged within electrocatalytic charge transfer at the 2nd interface (Scheme 2).

D describes how fast urea is able to reach active centers.[23] *D* values were calculated from eqn (2) based on the slopes determined from dependencies presented in Fig. 10b and 11b. For poly[NP-Ni(OH)$_2$SaltMe]$_{1\ M}$ and poly[*meso*-NP-Ni(OH)$_2$SaldMe]$_{1\ M}$, the calculated *D* values were: 5.87 × 10^{-7} cm^2 s^{-1} and 7.49 × 10^{-7} cm^2 s^{-1}, respectively. A higher *D* value obtained for urea reaching the poly(*meso*-NP-Ni^{3+}-OOHSaldMe)$_{1\ M}$ active sites indicated that a spatially diversified molecular structure of poly[*meso*-NP-Ni(OH)$_2$-SaldMe]$_{1\ M}$ facilitated the electrocatalytic process.

The Tafel slopes were determined to distinguish which structured poly[NP-Ni(OH)$_2$salen] catalyst produces catalytic current more efficiently in response to change in applied potential. The Tafel slopes determined for poly[NP-Ni(OH)$_2$SaltMe]$_{1\ M}$ and poly[*meso*-NP-Ni(OH)$_2$SaldMe]$_{1\ M}$ catalysts (Fig. 12) operating in the solution containing 0.3 M urea and 1.0 M NaOH$_{aq}$ were 25 mV dec^{-1} and 20 mV dec^{-1}, respectively. A lower Tafel slope obtained for poly[*meso*-NP-Ni^{3+}OOHSaldMe]$_{1\ M}$ indicates that for this catalyst there is a significant current density increment as a function of the overpotential change, or in other words, this catalyst produces catalytic current more efficiently in response to change in applied potential than poly[NP-Ni(OH)$_2$SaltMe]$_{1\ M}$. Furthermore, the obtained Tafel slopes are lower than those reported for other well-performing urea electrooxidation catalysts.[18,19,58]

To compare the E_{ac} values of urea electrooxidation on poly[NP-Ni(OH)$_2$SaltMe]$_{1\ M}$ and poly[*meso*-NP-Ni(OH)$_2$-SaldMe]$_{1\ M}$ and study the influence of temperature on the overall two-step catalytic process, the CV responses in 1.0 M NaOH$_{aq}$ were registered in the absence (Fig. S10†) and the presence of 0.3 urea (Fig. 13) at different temperatures (16, 19, 24, 28, 33, 38, and 43 °C). The control experiment performed in the absence of urea showed that with the temperature increase, the peak current slightly increased together with the peak potential decrease for poly[NP-Ni(OH)$_2$SaltMe]$_{1\ M}$ (Fig. S10a†), indicating more efficient generation of active sites at higher temperatures.

A similar behavior was observed for poly[*meso*-NP-Ni(OH)$_2$-SaldMe]$_{1\ M}$ but only for temperatures below 28 °C (Fig. S10b†). Further temperature increase led to a decrease in peak current coupled with the shift of peak potential to a higher value, thus suggesting hindered dedoping of OH$^-$ from poly(*meso*-NP-Ni^{3+}OOHSaldMe)$_{1\ M}$ active sites (Fig. S10b†). This hindered dedoping of OH$^-$ counterions was associated with a more spatially diversified structure of matrix templating active centers in 3D. In the presence of 0.3 M urea, with the temperature increase, the catalytic peak currents and the onset potentials decreased for both studied catalysts (Fig. 13), thus indicating the facilitated electrooxidation of urea at higher temperatures. A shift of the catalytic peak potential from 0.49 V to 0.66 V for poly[NP-Ni(OH)$_2$SaltMe]$_{1\ M}$ (Fig. 13a) and from 0.55 V to 0.67 V for poly[*meso*-NP-Ni(OH)$_2$SaldMe]$_{1\ M}$ (Fig. 13b) was observed. Because in the control experiment, we did not observe hindered desorption of OH$^-$ for poly[NP-Ni(OH)$_2$SaltMe]$_{1\ M}$ for all studied temperatures, thus the catalytic peak potential shift is undeniably attributed to the electrooxidation product accumulation. However, in the case of poly(*meso*-NP-Ni^{3+}-OOHSaldMe)$_{1\ M}$, the catalytic peak potential shift is attributed to hindered desorption of OH$^-$, which is supported by the control experiment (Fig. S10b†). The observed hindered dedoping of OH$^-$ ions from spatially expanded poly(*meso*-NP-Ni^{3+}OOHSaldMe)$_{1\ M}$ positively influences the final desorption of catalysis products. This result remains consistent with earlier analysis of the *in situ* generation/retention ability of poly(NP-Ni^{3+}OOHsalen) centers.

Arrhenius plots were prepared for potentials 0.45 and 0.5 V at different temperatures for urea electrooxidation. These plots showed a linear relation (Fig. 14), indicating no change in the two-step indirect urea oxidation mechanism for all studied temperatures.[59] E_{ac} was determined from Arrhenius plots according to eqn (6):

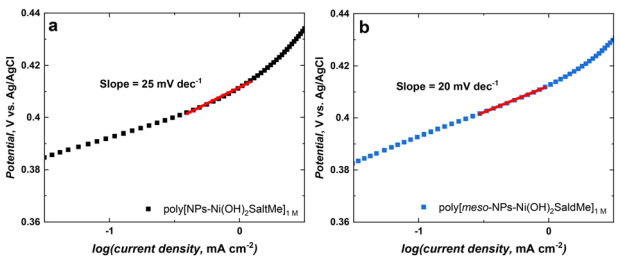

Fig. 12 Tafel slopes determined for (a) poly[NP-Ni(OH)$_2$SaltMe]$_{1\ M}$ and (b) poly[*meso*-NP-Ni(OH)$_2$SaldMe]$_{1\ M}$ catalysts operating in the solution containing 0.3 M urea and 1.0 M NaOH$_{aq}$.

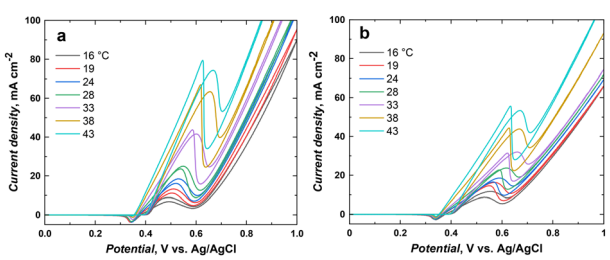

Fig. 13 Electrocatalytic CV responses of (a) poly[NP-Ni(OH)$_2$SaltMe]$_{1\ M}$ and (b) poly[*meso*-NP-Ni(OH)$_2$SaldMe]$_{1\ M}$ performed at different temperatures in the solution containing 0.3 M urea and 1.0 M NaOH$_{aq}$.

$$\frac{\partial \log(I)}{\partial \frac{1}{T}} = \frac{-E_{ac}}{2.3R} \quad (6)$$

where I is the current density, T is the temperature, and R is the gas constant. The calculated E_{ac} was lower for poly[*meso*-NP-Ni(OH)$_2$SaldMe]$_{1\ M}$ (20.82 and 21.35 kJ mol^{-1} for potentials 0.45 and 0.50 V, respectively) than for poly[NP-Ni(OH)$_2$SaltMe]$_{1\ M}$ (21.60 and 33.36 kJ mol^{-1} for potentials 0.45 and 0.50 V, respectively). These determined E_{ac} values indicated that poly[*meso*-NP-Ni(OH)$_2$SaldMe]$_{1\ M}$ exhibits higher catalytic activity than poly[NP-Ni(OH)$_2$SaltMe]$_{1\ M}$ toward urea electrooxidation.

Long-term stability test under real-system mimicking conditions

Chronoamperometric experiments were performed to mimic the operating conditions of the anode of the artificial urine and urea fuel cells. During these experiments, a constant potential was kept for 17 h in 1.0 M NaOH$_{aq}$ medium, ensuring progressing electrocatalytic oxidation of urea (i) from its pristine form (Fig. 15) or (ii) from artificial urine (Fig. 16) on the poly[NP-Ni(OH)$_2$SaltMe]$_{1\ M}$ and poly[*meso*-NP-Ni(OH)$_2$SaldMe]$_{1\ M}$ anodes. The same conditions were applied in the control experiment, where poly[NP-Ni(OH)$_2$-SaltMe]$_{1\ M}$ and poly[*meso*-NP-Ni(OH)$_2$SaldMe]$_{1\ M}$ were continuously electrooxidized to poly(NP-Ni^{3+}OOHSaldMe)$_{1\ M}$ and poly(*meso*-NP-Ni^{3+}OOHSaldMe)$_{1\ M}$, respectively. Under these conditions, the amount of electrogenerated poly(NP-Ni^{3+}OOHsalen) centers was constant and unchanged for both studied materials (Fig. 15, red curves). After urea addition, the sustenance of active poly(NP-Ni^{3+}OOHSaldMe) species throughout the pending reaction remains unaccomplished because of the indirect mechanism that involves the reduction of poly(NP-Ni^{3+}OOHsalen) into poly[NP-Ni^{2+}(OH)$_2$-salen] during electrocatalysis. The current retention values obtained after 15 h of pure urea electrooxidation on poly[NP-Ni(OH)$_2$SaltMe]$_{1\ M}$ and poly[*meso*-NP-Ni(OH)$_2$SaldMe]$_{1\ M}$ (Fig. 15) were ~44% and ~56% (Table S6†), respectively.

The respective retention values obtained for these catalysts operating in the presence of artificial urine were ~65% and ~70% (Fig. 16 and Table S6†). Poly[*meso*-NP-Ni(OH)$_2$SaldMe]$_{1\ M}$ indicated higher current retention in both analyzed cases. The high conductivity of artificial urine solution dissolved in 1 M NaOH$_{aq}$ enhanced the electrocatalytic current output (Fig. 16) compared to the current measured at 0.3 M urea in 1 M NaOH$_{aq}$ (Fig. 15).[60] Measurements in artificial urine helped check the proof of using the poly[NP-Ni(OH)$_2$salen] catalysts for urea oxidation from urea-rich wastewater-like systems.

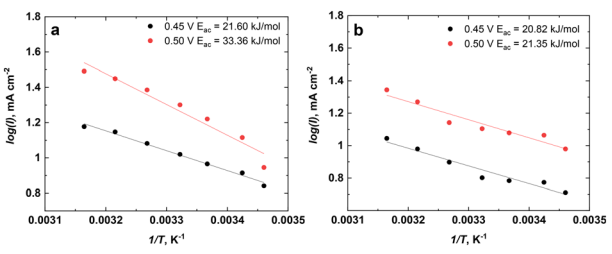

Fig. 14 Arrhenius plots prepared for (a) poly[NP-Ni(OH)$_2$SaltMe]1 M and (b) poly[*meso*-NP-Ni(OH)$_2$SaldMe]$_{1\ M}$ based on data from Fig. 13.

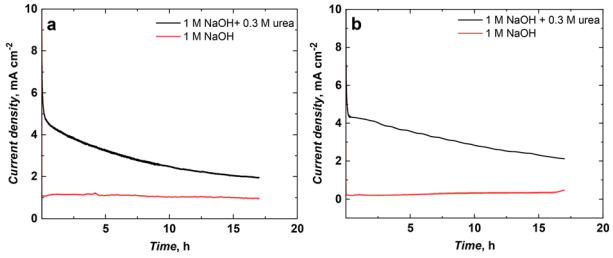

Fig. 15 Chronoamperometric measurements performed in 1.0 M NaOH$_{aq}$ in the absence (red) and presence (black) of 0.3 M urea for (a) poly[NP-Ni(OH)$_2$SaltMe]$_{1\ M}$ and (b) poly[*meso*-NP-Ni(OH)$_2$SaldMe]$_{1\ M}$ at a constant potential of 0.55 V *vs.* Ag/AgCl.

Conclusions

We optimized the best NaOH$_{aq}$ concentration used for the fabrication of two differently structured catalysts named poly[NP-Ni(OH)$_2$SaltMe]$_{1\ M}$ and poly[*meso*-NP-Ni(OH)$_2$SaldMe]$_{1\ M}$ active towards urea electrooxidation. A combination of SEM and TEM imaging supplemented by evaluating the poly(NP-Ni^{3+}OOHsalen) catalytic centers' *in situ* generation abilities according to the indirect urea electrooxidation mechanism was our criteria for choosing the best catalyst fabrication conditions. Recognition of the two-step indirect mechanism of electrocatalytic urea oxidation on poly[NP-Ni(OH)$_2$SaltMe]$_{1\ M}$ and poly[*meso*-NP-Ni(OH)$_2$SaldMe]$_{1\ M}$ imposed a need for finding the best possible catalytic conditions. Hence we focused on finding the best NaOH$_{aq}$ and urea concentration for electrocatalysis. Both studied catalysts indicated the best performance in 1.0 M NaOH$_{aq}$ containing 0.3 M urea. Moreover, we elucidated the differences in the electrocatalytic performance of the fabricated catalysts using comprehensive electrochemical methodology. This methodology primarily involved electrochemical control studies differentiating the indirect two-step process of urea oxidation, determination of

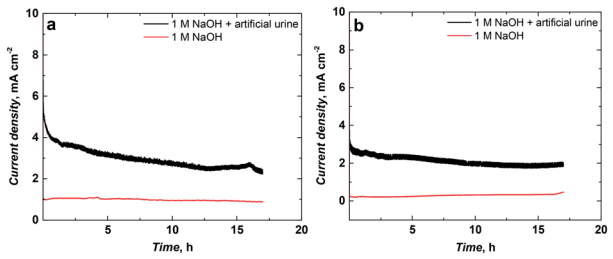

Fig. 16 Chronoamperometric measurements performed in 1.0 M NaOH$_{aq}$ in the absence (red) and the presence (black) of artificial urine containing 0.25 M urea for (a) poly[NP-Ni(OH)$_2$SaltMe]$_{1\ M}$ and (b) poly[*meso*-NP Ni(OH)$_2$SaldMe]$_{1\ M}$ at the constant potential of 0.55 V *vs.* Ag/AgCl.

urea diffusion coefficients, Tafel slope analysis, and activation energy studies. Finally, we elucidated the differences in structure-related performance of poly[NP-Ni(OH)$_2$SaltMe]$_{1\ M}$ and poly[*meso*-NP-Ni(OH)$_2$SaldMe]$_{1\ M}$. These catalysts featured different placements of active center arrangements, *i.e.*, poly[NP-Ni(OH)$_2$SaltMe]$_{1\ M}$ active centers remained mainly on the catalyst surface, while poly[*meso*-NP-Ni(OH)$_2$SaldMe]$_{1\ M}$ active centers were distributed in the catalyst bulk. It turned out that the high spatial distribution of poly(NP-Ni^{3+}-OOHSaldMe)$_{1\ M}$ catalytically active sites caused their better sustenance during electrocatalytic urea oxidation. This was also reflected in the high retention of catalytic current obtained for poly(NP-Ni^{3+}OOHSaldMe)$_{1\ M}$ when operating in real-system mimicking conditions. Moreover, the Tafel slope of 20 mV dec^{-1} and E_a of 20.82 kJ mol^{-1} confirmed that this bulk-structured catalyst is efficient and highly active towards UOR.

Data availability

The authors confirm that the data supporting the findings of this study are available within the article and/or in its ESI.†

Author contributions

Monika Mierzejewska: electrochemical experiments, writing. Kamila Łępicka: conceptualization, Ni-salen monomer synthesis, writing. Jakub Kalecki: SEM imaging. Piyush Sindhu Sharma: project management, editing and writing.

Conflicts of interest

There are no conflicts to declare.

Acknowledgements

The authors thank Dr Kamil Sobczak (Biological and Chemical Research Centre, University of Warsaw) for TEM analysis. The present research was financially supported by the National Science Center (Poland) through Grant No. 2018/29/B/ST5/02335 to PSS.

References

1 R. K. Singh, K. Rajavelu, M. Montag and A. Schechter, *Energy Technol.*, 2021, **9**, 2100017.
2 A. Coombs, *Nature*, 2008, 2578.
3 E. T. Sayed, T. Eisa, H. O. Mohamed, M. A. Abdelkareem, A. Allagui, H. Alawadhi and K.-J. Chae, *J. Power Sources*, 2019, **417**, 159–175.
4 J. Li, S. Wang, S. Sun, X. Wu, B. Zhang and L. Feng, *J. Mater. Chem. A*, 2022, **10**, 9308–9326.
5 Y. M. T. A. Putri, J. Gunlazuardi, Y. Yulizar, R. Wibowo, Y. Einaga and T. A. Ivandini, *Open Chem.*, 2021, **19**, 1116–1133.
6 S. Lu, M. Hummel, Z. Gu, Y. Wang, K. Wang, R. Pathak, Y. Zhou, H. Jia, X. Qi, X. Zhao, B. B. Xu and X. Liu, *ACS Sustainable Chem. Eng.*, 2021, **9**, 1703–1713.
7 B. Zhu, Z. Liang and R. Zou, *Small*, 2020, **16**, 1906133.
8 E. Urbanczyk, M. Sowa and W. Simka, *J. Appl. Electrochem.*, 2016, **46**, 1011–1029.
9 W. Simka, J. Piotrowski and G. Nawrat, *Electrochim. Acta*, 2007, **52**, 5696–5703.
10 A. T. Miller, B. L. Hassler and G. G. Botte, *J. Appl. Electrochem.*, 2012, **42**, 925–934.
11 R. L. King and G. G. Botte, *J. Power Sources*, 2011, **196**, 9579–9584.
12 A. Kumar, X. Liu, J. Lee, B. Debnath, A. R. Jadhav, X. Shao, V. Q. Bui, Y. Hwang, Y. Liu, M. G. Kim and H. Lee, *Energy Environ. Sci.*, 2021, **14**, 6494–6505.
13 B. K. Boggs, R. L. King and G. G. Botte, *Chem. Commun.*, 2009, 4859–4861.
14 H. Kim, T. Y. Yoo, M. S. Bootharaju, J. H. Kim, D. Y. Chung and T. Hyeon, *Adv. Sci.*, 2022, **9**, 2104054.
15 M. A. Goda, M. G. A. El-Moghny and M. S. El-Deabz, *J. Electrochem. Soc.*, 2020, **167**, 064522.
16 F. Wu, G. Ou, J. Yang, H. Li, Y. Gao, F. Chen, Y. Wang and Y. Shi, *Chem. Commun.*, 2019, **55**, 6555–6558.
17 L. Xia, Y. Liao, Y. Qing, H. Xu, Z. Gao, W. Li and Y. Wu, *ACS Appl. Energy Mater.*, 2020, **3**, 2996–3004.
18 L. Jin, R. Ji, H. Wan, J. He, P. Gu, H. Lin, Q. Xu and J. Lu, *ACS Catal.*, 2023, **13**, 837–847.
19 N. N. Rao, C. Alex, M. Mukherjee, S. Roy, A. Tayal, A. Datta and N. S. John, *ACS Catal.*, 2024, **14**, 981–993.
20 Y. Tong, P. Chen, M. Zhang, T. Zhou, L. Zhang, W. Chu, C. Wu and Y. Xie, *ACS Catal.*, 2018, **8**, 1–7.
21 R. P. Forslund, C. T. Alexander, A. M. Abakumov, K. P. Johnston and K. J. Stevenson, *ACS Catal.*, 2019, **9**, 2664–2673.
22 R. P. Forslund, J. T. Mefford, W. G. Hardin, C. T. Alexander, K. P. Johnston and K. J. Stevenson, *ACS Catal.*, 2016, **6**, 5044–5051.
23 V. Vedharathinam and G. G. Botte, *Electrochim. Acta*, 2012, **81**, 292–300.
24 G. Hopsort, D. P. D. Carmo, L. Latapie, K. Loubière, K. G. Serrano and T. Tzedakis, *Electrochim. Acta*, 2023, **442**, 141898.
25 R. K. Singh and A. Schechter, *Electrochim. Acta*, 2018, **278**, 405–411.
26 R. M. Abdel Hameed and S. S. Medany, *Int. J. Hydrogen Energy*, 2019, **44**, 3636–3648.
27 S. Wang, P. Xu, J. Tian, Z. Liu and L. Feng, *Electrochim. Acta*, 2021, **370**, 137755.
28 C. Alex, G. Shukla and N. S. John, *Electrochim. Acta*, 2021, **385**, 138425.
29 V. Vedharathinam and G. G. Botte, *Electrochim. Acta*, 2013, **108**, 660–665.
30 M. Mazloum-Ardakani, V. Eslami and A. Khoshroo, *Mater. Sci. Eng., B*, 2018, **229**, 201–205.
31 M. Mierzejewska, K. Łępicka, J. Kalecki, W. Lisowski and P. S. Sharma, *ACS Appl. Mater. Interfaces*, 2022, **14**, 33768–33786.
32 W. Wang, D. Chai, J. Zhang, S. Xue, Y. Wang and Z. Lei, *J. Taiwan Inst. Chem. Eng.*, 2017, **80**, 326–332.

33 D. A. Daramola, D. Singh and G. G. Botte, *J. Phys. Chem. A*, 2010, **114**, 11513–11521.
34 L. F. Huang, M. J. Hutchison, R. J. Santucci Jr., J. R. Scully and J. M. Rondinelli, *J. Phys. Chem. C*, 2017, **121**, 9782–9789.
35 M. Pourbaix, *Atlas of Electrochemical Equilibria*, National Association of Corrosion Engineers, Houston, Texas, USA, 1974.
36 S. Lu, X. Zheng, L. Fang, F. Yin and H. Liu, *Electrochem. Commun.*, 2023, 107599.
37 X. Hu, J. Zhu, J. Li and Q. Wu, *ChemElectroChem*, 2020, **7**, 3211–3228.
38 J. Ge, J. Kuang, Y. Xiao, M. Guan and C. Yang, *Surf. Interfaces*, 2023, **41**, 103230.
39 N. Kuznetsov, P. Yang, G. Gorislov, Y. Zhukov, V. Bocharov, V. Malev and O. Levin, *Electrochim. Acta*, 2018, **271**, 190–202.
40 J. L. Bott-Neto, T. S. Martins, S. R. A. S. Machado and E. A. Ticianelli, *ACS Appl. Mater. Interfaces*, 2019, **11**, 30810–30818.
41 A. Olean-Oliveira, C. F. Pereira, D. N. David-Parra and M. F. S. Teixeira, *ChemElectroChem*, 2018, **5**, 3557–3565.
42 M. Vilas-Boas, C. Freire, B. de Castro and A. R. Hillman, *J. Phys. Chem. B*, 1998, **102**, 8533–8540.
43 K. Łępicka, P. Pieta, A. Shkurenko, P. Borowicz, M. Majewska, M. Rosenkranz, S. Avdoshenko, A. A. Popov and W. Kutner, *J. Phys. Chem. C*, 2017, **121**, 16710–16720.
44 N. Sarigul, F. Korkmaz and İ. Kurultak, *Sci. Rep.*, 2019, **9**, 20159.
45 K. Łępicka, P. Pieta, R. Gupta, M. Dabrowski and W. Kutner, *Electrochim. Acta*, 2018, **268**, 111–120.
46 E. Laviron, *J. Electroanal. Chem. Interfacial Electrochem.*, 1979, **101**, 19–28.
47 L. M. F. Dantas, A. P. D. Reis, S. M. C. N. Tanaka, J. H. Zagal, Y.-Y. Chen and A. A. Tanaka, *J. Braz. Chem. Soc.*, 2008, **19**, 720–726.
48 A. Bard and L. Faulkner, *Electrochemical Methods. Fundamentals and Applications*, John Wiley & Sons, New York, 2nd edn, 2001.
49 M. Vilas-Boas, C. Freire, B. de Castro and A. R. Hillman, *J. Phys. Chem. B*, 1998, **102**, 8533–8540.
50 M. Vilas-Boas, C. Freire, B. de Castro, P. A. Christensen and A. R. Hillman, *Inorg. Chem.*, 1997, **36**, 4919–4929.
51 M. Vilas-Boas, C. Freire, B. de Castro, P. A. Christensen and A. R. Hillman, *Chem. – Eur. J.*, 2001, **7**, 139–150.
52 R. Lin, L. Kang, T. Zhao, J. Feng, V. Celorrio, G. Zhang, G. Cibin, A. Kucernak, D. J. L. Brett, F. Cora, I. P. Parkin and G. He, *Energy Environ. Sci.*, 2022, **15**, 2386–2396.
53 C. Batchelor-McAuley, *Curr. Opin. Electrochem.*, 2023, **37**, 101176.
54 R. Sanchis-Gual, A. Seijas-Da Silva, M. Coronado-Puchau, T. F. Otero, G. Abellán and E. Coronado, *Electrochim. Acta*, 2021, **388**, 138613.
55 X. Gao, X. Bai, P. Wang, Y. Jiao, K. Davey, Y. Zheng and S.-Z. Qiao, *Nat. Commun.*, 2023, **14**, 5842.
56 K. Aoki, K. Tokuda and H. Matsuda, *J. Electroanal. Chem. Interfacial Electrochem.*, 1983, **146**, 417–424.
57 J. O. M. Bockris and S. U. M. Khan, *Surface Electrochemistry, A Molecular Level Approach*, Springer New York, Plenum Press, New York and London, 1993.
58 Z. Ji, Y. Song, S. Zhao, Y. Li, J. Liu and W. Hu, *ACS Catal.*, 2022, **12**, 569–579.
59 J. Masa, S. Barwe, C. Andronescu and W. Schuhmann, *Chem. – Eur. J.*, 2019, **25**, 158–166.
60 C. Santoro, M. J. S. Garcia, X. A. Walter, J. You, P. Theodosiou, I. Gajda, O. Obata, J. Winfield, J. Greenman and I. Ieropoulos, *ChemElectroChem*, 2020, **7**, 1312–1331.